Journal Name

ARTICLE TYPE

Cite this: DOI: 00.0000/xxxxxxxxxx

Laser Initiated Site-selective Formation of Fluorescing $Ag-Fe_2O_3$ Nanocomposites for Electron Detection†

Yue Yin[a], Aseera Jannath[a], Zheng Zhang[b], Chorng Haur Sow*[c] and Sharon Xiaodai Lim*[c]

Received Date
Accepted Date

DOI: 00.0000/xxxxxxxxxx

There has been continual interest in the fabrication of $Ag-Fe_2O_3$ composite nanostructures due to its effectiveness in antimicrobial, catalytic and sensing applications. However, traditional processes involve multiple steps and harsh conditions, making them time consuming and energy intensive. A focused laser beam is used as an alternative tool to fabricate fluorescing $Ag-Fe_2O_3$ composite nanostructures. The rapid thermal annealing and quenching process leads to uniformly distributed particles that form site-selectively in the lasered regions. Performed without demanding conditions or any additives, this process is more precise, energy and cost-efficient compared to traditional methods. Presence of Ag within the composite enhances the intrinsic fluorescence of Fe_2O_3 by more than 10 times through surface plasmon resonance effects. This exclusive trait turns the composite into an effective micro-beta particle detector with in-situ optical feedback. This work offers a glimpse to the benefits of developing alternative synthesis processes as a means to uncover alternative applications.

1 Introduction

The synthesis of silver- iron (III) oxide ($Ag-Fe_2O_3$) nanostructures has attracted continued interest due to its effectiveness in biomedical[1], environmental remediation[2], catalysis[3], and sensing applications. As an antimicrobial agent, $Ag-Fe_2O_3$ it is particularly effective due to the synergistic effects of silver and its Fe_2O_3 substrate[4]. They are also used in the catalytic degradation of water pollutants[2,3,5], and to detect CO, NO, and volatile organic compounds (VOCs)[4].

Many methods have been explored over the years for the synthesis of the $Ag-Fe_2O_3$ nanocomposite. Traditional methods include the sol-gel method[4], the hydrothermal method[6] and the co-precipitation method[2]. More recently, much effort has been devoted to the development of green synthesis methods using biological extracts[7–10]. The sol-gel method offers the benefit of good control over particle size and homogeneity. However, it can be costly due to its requirements for specific precursors, controlled environments, and stabilising agents to be added.

Furthermore, such processes are energy-intensive due to the drying and calcination processes conducted at high temperatures. The hydrothermal method also provides good control over particle morphology and size, but it also suffers from high energy consumption due to the need to maintain elevated temperatures and pressures. Co-precipitation can be cheap and scalable, but offers limited control over size and morphology. The process of co-precipitation also requires the addition of chemical surfactants and stabilisers. While green synthesis methods improve traditional precipitation methods by substituting more eco-friendly biological extracts for chemical reducing agents and stabilisers, the process suffers from the same limitations regarding inhomogeneous size and morphology.

This work attempts to address the above limitations by exploring a different avenue for synthesising the $Ag-Fe_2O_3$ nanocomposite. A focused laser beam initiates the site-selective photothermal reduction of aqueous Ag^+ ions. The strong but localised heating allows $Ag-Fe_2O_3$ nanocomposites to be formed evenly under ambient conditions without surfactants or stabilising additives. As a result, the process is a cost and energy-efficient alternative to traditional methods. Relatively good control over particle size and morphology is also achieved. Furthermore, this method has the distinctive feature of site-selectivity, that is, the formation of the nanocomposite is controlled within the site of the laser treatment only. This facilitates the precision engineering of highly specific arrangements of the nanostructure to micrometre precision, and as we enter an age of micro- and nano-sized devices and lab-on-a-chip applications, the ability to conduct precise directed assembly of various micro- and nano-structures could be increasingly valuable[11].

[a] Raffles Institution, 1 Raffles Institution Lane, Singapore 575954
[b] Institute of Materials Research and Engineering (IMRE), Agency for Science, Technology and Research (A*STAR), 2 Fusionopolis Way, Innovis #08-03, Singapore 138634, Singapore.
[c] Department of Physics, National University of Singapore, 2 Science Drive 3, Singapore 117542. Tel: +65 6516 1161; Fax number: (65) 6777 6126; E-mail: phylimx@nus.edu.sg

† Supplementary Information available: Image processing pipeline for size distribution analyses; Plot of change in fluorescence intensity with different amount of electron dosage; Video of bubble formation during lasering under $AgNO_3$, and Video of no bubble formation during lasering under de-ionised water. See DOI: 00.0000/00000000.

Uniquely, the Ag−Fe_2O_3 nanocomposite formed emits strong red fluorescence under yellow excitation. This fluorescing phenomenon is due to Ag amplifying the intrinsic red fluorescence of the crystalline Fe_2O_3 nanoflakes by more than 10 times. The fluorescence property thus serves as a simple and reliable means of determining successful nanocomposite formation without requiring more expensive characterisation. While characterising the composite material, the fabricated nanocomposite reacts to electron irradiation with an increase in its fluorescence intensity after being exposed to an electron beam.

Through determining the composition of irradiated and non-irradiated samples, as well as an in-situ observation of the nanostructure's changes during electron irradiation on an atomic level under the TEM, the mechanism of this change is identified to be due to the solid-state reduction of silver oxides into silver by electron bombardment. In other words, the fluorescence from the Ag−Fe_2O_3 nanocomposite can response to the changes in the oxidation state of the Ag. This unique property illuminates the possibility of new applications for this well-known nanocomposite: (i) a micro-beta particle detector with real-time optical feedback, or (ii) a pathway for developing cheap, non-destructive optical probing capable of monitoring the degradation of silver catalysts and plasmonic devices. This work thus highlights the benefits of developing alternative processes for fabricating traditional materials, which lies in the potential of uncovering unique features and applications.

2 Experiments

2.1 Materials and Methods

2.1.1 Formation of Iron (III) Oxide Nanoflakes Substrate

Single-crystalline iron (III) oxide (Fe_2O_3) nanoflakes are synthesised using the hotplate method[12]. Iron foil (Aldrich, 0.025 mm thick) is polished to remove surface oxidation and cleaned with isopropanol. It is then placed on a hotplate (Thermofisher) and heated directly in air at 400 °C for varying durations (1, 3, 6, 10, and 20 hours).

2.1.2 Further Characterisation

Further characterisations are carried out using: Fluorescence microscopy (FM, Olympus BX51) under Bright Field (BF) light and yellow (530-580 nm) wavelength light excitation. Raman spectroscopy and photoluminescence (PL) spectroscopy (Renishaw inVia Qontor with 532 nm lasers). Transmission electron microscopy (TEM, JEOL 2010F). Scanning electron microscopy (SEM, JEOL JSM6700-F) and energy dispersive X-ray spectroscopy (EDX, Oxford Instruments X-MaxN 150). X-ray photoelectron (XPS) spectroscopy analyses are carried out using Thermofisher Scientific Theta Probe XPS with monochromatic Al K alpha X-ray (1486.7 eV) with charge correction for binding energy based on C 1s from adventitious carbon at 285.0 eV.

3 Results and Discussion

3.1 Formation of Iron (III) Oxide Nanoflakes

Iron (III) oxide (Fe_2O_3) nanoflakes are grown *via* the solid-liquid-solid growth mechanism. When the temperature of the hotplate is sufficiently high, the surface layer of the iron foil begins to melt, forming a liquid medium. Subsequently, the liquid medium adsorbs the oxygen in the air and is oxidised to iron (II, III) oxide (Fe_3O_4), which acts as the precursor for the growth of the Fe_2O_3 nanoflakes. Fe_2O_3 forms when the surface Fe_3O_4 is further oxidised, and Fe_2O_3 precipitates from the liquid medium after supersaturation. The growth continues until it cools down, condensing the liquid to the solid state[12].

SEM images of the Fe_2O_3 nanoflakes after varying heating durations are shown in Figure 1(a), with the corresponding optical images as insets. Before heating, the pristine iron foil has a smooth and silvery appearance. Under SEM, it appears roughened (which is due to the sanding) but is not jagged. Referring to the inset for 1 hour of heating, a layer with the characteristic reddish brown colouration of Fe_2O_3 can already be seen on the surface of the sample. The coverage density of this layer increases as the heating duration increases, causing the samples to appear darker visually. Under SEM, thin jagged Fe_2O_3 nanoflakes are formed under shorter heating durations, and they gradually become smoother, rounder and more uniform as the heating duration increases from 1 to 20 hours. Since they produced the most uniform Fe_2O_3 nanoflakes, 20 hours of heat treatment was chosen for further investigation.

Elemental analysis is conducted on the nanoflake sample heated for 20 hours. EDX elemental map reveals a uniform distribution of iron and oxygen elements across the samples (Figure 1(b)). The result highlights the uniformity achieved through the simple hotplate-assisted synthesis process. Complementing the EDX analysis is the Raman spectrum of the Fe_2O_3 nanoflake sample as shown in Figure 1(c). The Raman spectrum shows the characteristic peaks of Fe_2O_3 at 229 cm^{-1}, 294 cm^{-1}, 410 cm^{-1}, 499 cm^{-1}, 609 cm^{-1} and 1315 cm^{-1} [13], where the peaks at 229 cm^{-1} and 499 cm^{-1} correspond to the A_{1g} vibrational mode and the peaks at 294 cm^{-1}, 410 cm^{-1} and 609 cm^{-1} to the E_g vibrational mode[14]. The 1315 cm^{-1} peak is due to a second-order scattering process and is specific for the two-phonon or two-magnon scattering process in the Fe_2O_3 nanoflakes[15]. These peaks thus verified the successful formation of the Fe_2O_3 nanoflakes *via* the hotplate synthesis process. It can be noted that there is also a peak at 662 cm^{-1} not traditionally associated with Fe_2O_3. This peak is close to that of magnetite (Fe_3O_4)'s main Raman peak and may be attributed to incomplete phase transformation[16,17].

The crystallinity of the synthesized Fe_2O_3 nanoflake sample is determined by TEM analysis (Figure 1(d)). Under lower magnification in Figure 1(d(i)), it can be seen that the nanoflakes have sharp and well-defined edges. The high resolution TEM (HRTEM) image of the region shown in Figure 1(d(ii)) had a measured lattice spacing of 2.83 Å, corresponding to the hexagonal primitive Fe_2O_3 (113) plane (JCPDS PDF #40-1139). The bright, distinct spots arranged in a periodic manner obtained in the selected area electron diffraction (SAED) pattern (Figure 1(d(iii))) indicate good crystallinity with single orientation. By analysing the d-spacing and angle between the planes, the SAED pattern was matched to the (1 0 11) and (2 0 1) planes of a hexagonal primitive Fe_2O_3 crystal structure.

Fe 2p and O 1s XPS of the sample are also reported in Figure

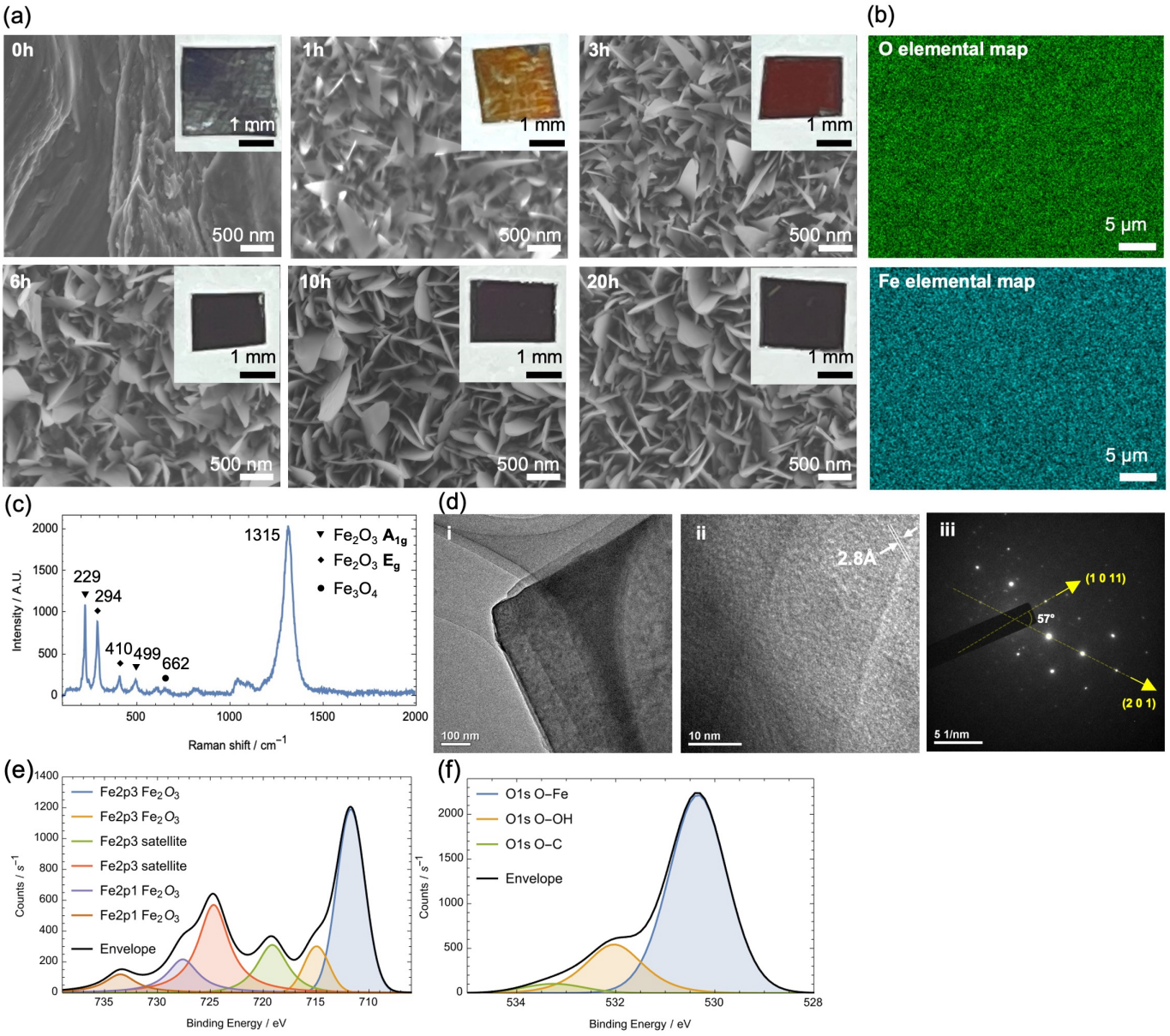

Fig. 1 (a) SEM images of the Fe_2O_3 nanoflakes formed after 0, 1, 3, 6, 10 and 20 hours of growth, with corresponding optical images in the inset. (b) EDX elemental map of elements O and Fe, (c) Raman spectrum, (d)(i) TEM image, (ii) High resolution TEM (HRTEM) image, (iii) SAED and (e-f) XPS showing (e) Fe 2p and (f) O 1s scans from the Fe_2O_3 nanoflakes after 20 hours of growth.

1(e) and 1(f), respectively. As expected, signals at 712 eV, 715 eV, 727.5 eV, and 733.5 eV attributed to bonding electrons of iron in Fe_2O_3 are obtained, as well as a strong peak at 530.3 eV due to the O1s electrons involved in O-Fe bonding. There are also much weaker peaks from O-OH and O-C bonds, which are likely attributed to water and carbon dioxide adsorbed onto the sample's surface.

3.2 Laser-Initiated Photo-Reduction of Silver on Iron (III) Oxide Nanoflakes

Following the successful growth of the Fe_2O_3 nanoflakes, a focused laser beam (FLB) setup is used to initiate the formation of the Ag–Fe_2O_3 nanocomposite. The formation process occurs *via* laser-assisted photothermal reduction of silver nitrate solution in the presence of the Fe_2O_3 substrate. A schematic of the laser set-up is shown in Figure 2(a). A green diode laser (532 nm) is used in this setup. The laser beam is first passed through a neutral density filter that facilitates fine tuning of the beam intensity, then reflected into an optical microscope using two plane mirrors. A dichroic mirror then redirects the laser to be focused *via* the 100x objective lens into a spot of diameter 1.5 μm. The sample is affixed to a glass slide using a small piece of double-sided tape and then placed on a MICOS X-Y stage controlled by Microsoft Visual Basic software.

A thin piece of 1:12 base to curing agent (w:w) polydimethylsiloxane (PDMS) polymer forms a well to ensure the silver nitrate

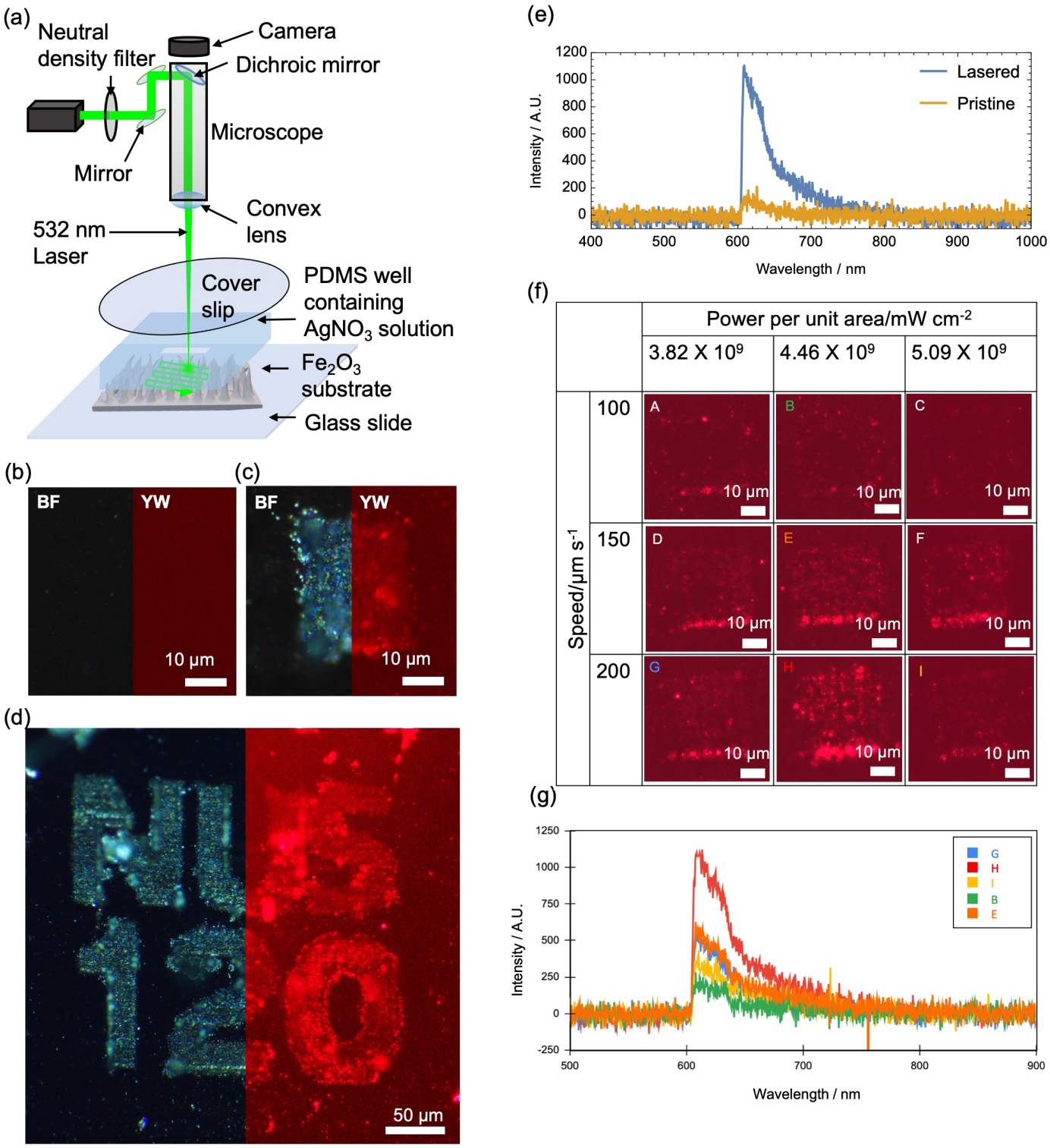

Fig. 2 (a) Schematic of the focused laser beam set-up. (b) Pristine sample and (c) lasered micro square under bright field (left) and yellow excitation (right). (d) Micro pattern of words "NUS 120" observed under bright field (left) and yellow excitation (right). (e) FM spectra of pristine and lasered samples under yellow excitation. (f) FM images of lasered squares with various lasering parameters and (g) the corresponding fluorescence spectra from (f).

solution remains in contact with the underlying substrate. To do so, a rectangular piece was cut out from its centre to form a well before the polymer is placed on top of the Fe_2O_3 nanoflake substrate. A micro-pipette fills this well with 0.1 M concentration of silver nitrate solution. Lastly, a glass cover slip is placed over the PDMS well to eliminate the possibility of laser attenuation due to meniscus formation. Laser treatment of the Fe_2O_3 substrate in an aqueous silver nitrate environment is achieved by focusing

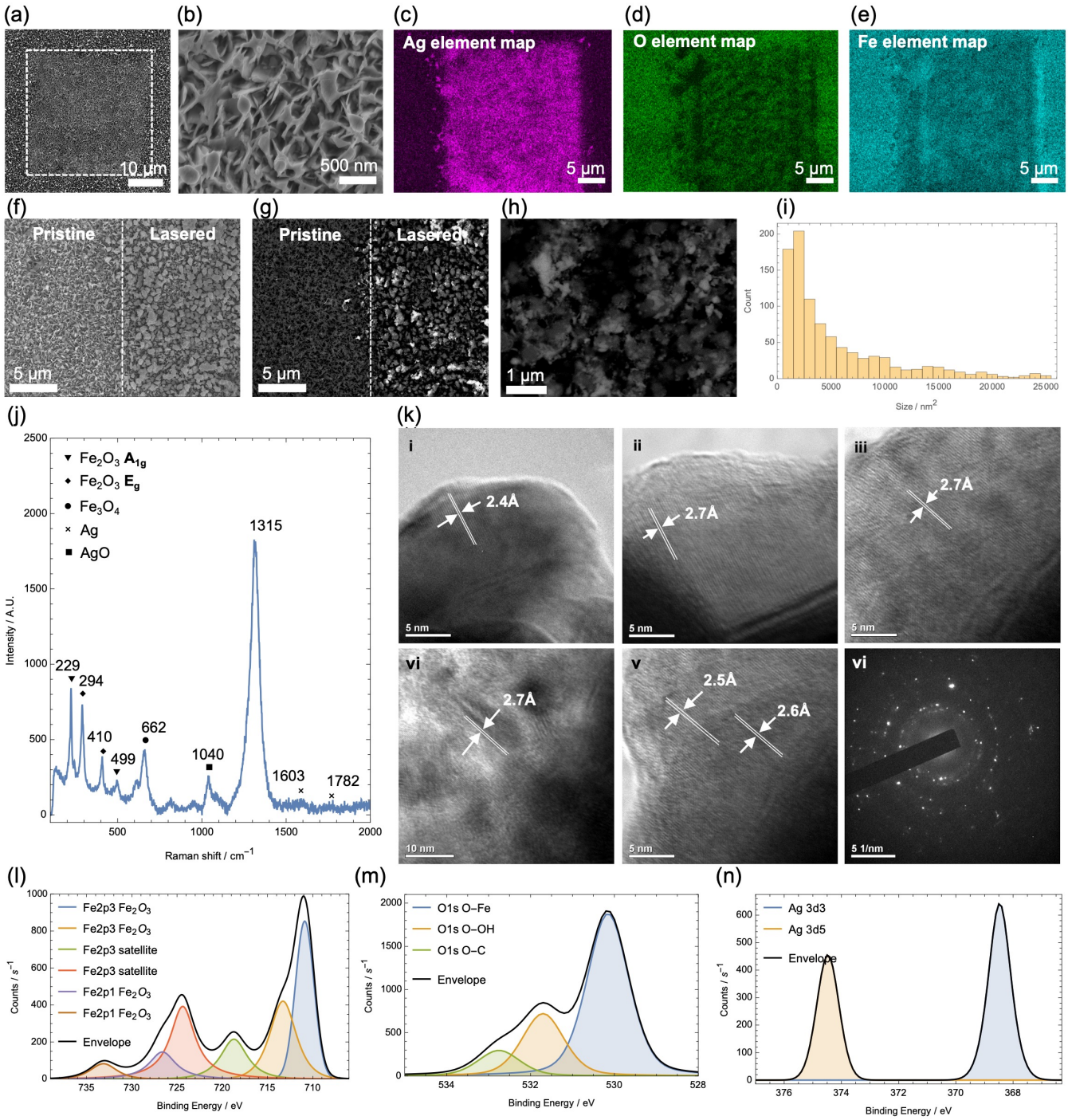

Fig. 3 (a-b) Lasered square under SEM with secondary electron imaging (SEI) taken at (a) lower and (b) higher magnification. (c-e) EDX element map of (c) Ag, (d) O, and (e) Fe from the lasered square. (f) Pristine (left) and lasered (right) regions under SEM with secondary electron imaging, and (g) with backscatter electron (BSE) imaging of the same region. (h) Lasered region under SEM with BSE imaging at higher magnification. (i) Histogram showing size distribution of silver nanoparticle deposits. (j) Raman spectrum of the lasered region. (k)(i-v) HRTEM images of the Ag−Fe_2O_3 nanocomposite. (vi) SAED pattern of the nanocomposite. (l-n) XPS spectra of (l) Fe 2p, (m) O 1s, and (n) Ag 3d scans.

the laser beam on the substrate surface within the PDMS well. By varying the laser's intensity and patterning speed as it interacts with the sample, the degree of photothermal reduction of the silver nitrate solution in the presence of Fe_2O_3 can be tuned. This, in turn, changes the final chemical and physical properties of the Ag−Fe_2O_3nanocomposite formed.

The FLB was used to pattern 30 μm by 30 μm squares onto the sample with a raster motion, after which the lasered structures were observed under the FM. Figure 2(b) shows a typical optical image of the pristine sample. Viewed under bright field, the sample appears uniform and dark. However, it emits a dim red fluorescence under yellow excitation. An example of the lasered

square is shown in Figure 2(c). The formation of uniformly distributed bright blue specks within the lasered square region can be seen under bright field, and these bright blue specks correspond to points with bright red fluorescence under yellow excitation. To demonstrate how this deposition process has achieved site-selectivity in the formation of the silver-containing nanocomposite, a micro-pattern spelling out the words “NUS 120” was created and shown in Figure 2(d). Comparing the spectra obtained from the pristine and the lasered sample under yellow excitation (Figure 2(e)), a significant 10.7 times increase in the fluorescence intensity is observed from the lasered sample. This strongly suggests that non-destructive optical characterisation can be a viable means to determine the successful formation of the $Ag-Fe_2O_3$ composite.

3.3 Optimal Lasering Parameters

To determine the optimal parameter for the uniform synthesis of the $Ag-Fe_2O_3$ nanocomposite across the lasered region, laser power densities of 3.82×10^9, 4.46×10^9 and 5.09×10^9 $mW\,cm^{-2}$, as well as lasering speeds of 100, 150 and 200 $\mu m\,s^{-1}$ were systematically varied (Figure 2(f)). Since the incorporation of silver increased the red fluorescence observed, this would be indicative of more $Ag-Fe_2O_3$ nanocomposites formed in a uniform and controlled manner. Hence, fluorescence analysis is used to find the set of parameters that would yield the product with the brightest and most uniform fluorescence.

Through the optimisation process, a few important trends are noted. On one hand, at a lower laser power density (Figure 2(f) A, D, G), there is little visible fluorescence. This is likely due to the low rate of photon incidence, which limits the amount of Fe^{3+} and O^{2-} ions formed. The formation of these ions is critical in enabling the formation of the $Ag-Fe_2O_3$ nanocomposite. A more detailed discussion on the formation mechanism of this composite is presented in the subsequent section.

On the other hand, a higher laser power density (Figure 2(f) C, F, I), also resulted in a significant decrease in fluorescence. Unlike the phenomenon observed at a lower laser power density, the lack of fluorescence at higher laser powers could be due to substantial ablation of the Fe_2O_3 nanoflake layer, leading to the exposure of the underlying Fe foil. This hypothesis is supported by the EDX elemental mapping (Figure 3(d-e)), which demonstrated a marked reduction in the quantity of both Fe and O in the lasered region compared to the surrounding non-lasered region. This indicates that the underlying nanoflake substrate is ablated during the laser modification. Since the Fe_2O_3 nanoflakes are necessary for the formation of the fluorescent product, this causes the brightness to decrease at high powers. Finally, the uniformity of the fluorescence increases notably when the patterning speed increases, leading to an overall higher intensity. Similarly to the case with higher lasering power, at slower interaction speeds, there could be more significant ablation of the Fe_2O_3 nanoflake layer.

Quantification of the fluorescence observed under yellow excitation is achieved by analysing the area under the spectra obtained from individual squares (Figure 2(g)). The laser power density of 4.46×10^9 $mW\,cm^{-2}$ and a patterning speed of 200 $\mu m\,s^{-1}$ (Figure 2(f) H) was chosen for detailed characterisation as it yielded the brightest and most uniform fluorescence, indicated by the highest fluorescence peak (Figure 2(g)). The systematic study thus provided a means to identify the optimal parameter for the $Ag-Fe_2O_3$ nanocomposite formation. Thereafter, samples created under the optimal condition will be labelled as "lasered" and detailed characterisations with comparisons to pristine samples will be carried out.

Under the SEM, secondary electron imaging (SEI) was first used to observe the surface morphology of the $Ag-Fe_2O_3$ nanocomposites. Figure 3(a) shows the lasered square exhibiting a distinct morphological difference compared to the surrounding pristine region. The higher magnification image in Figure 3(b) shows the formation of spherical protrusions on the nanoflake tips in the lasered sample. The elemental mapping of Ag, O and Fe from the EDX analysis performed on the lasered square is reported in Figure 3(c-e). Ag is distributed only in the laser-patterned region, while there is a reduction in the density of Fe and O in the patterned region.

To conduct a statistical study on the size and distribution of the Ag nanoparticle protrusions formed, backscattered electron (BSE) imaging was conducted on the lasered sample. Figure 3(f) and (g) show the same region observed using secondary (f) and backscattered (g) electrons. Since Ag has a larger atomic mass than Fe_2O_3, the regions where Ag is present appear brighter under BSE, as shown in Figure 3(g). This allows them to be identified using a threshold filter. Image analysis is conducted using ImageJ[18], and more details can be found in the supplementary information image S1. 20 images taken under higher magnification using BSE, such as the one in Figure 3(h), were analysed, and a histogram of the size distribution of the Ag nanoparticles is plotted in Figure 3(i). The Ag nanoparticles follow a right-skewed distribution, with 80% of the particles falling below the size of 9000 nm^2.

Raman analysis (Figure 3(j)) of the lasered sample shows a strong peak at 1040 cm^{-1} which is attributed to Ag[19] and peaks at 1603 cm^{-1} and 1782 cm^{-1} attributed to AgO (Figure 3(k))[20]. Thus, demonstrating the successful formation of Ag and AgO on the Fe_2O_3 nanoflakes.

Subsequently, the lasered sample is imaged under the HRTEM, and the images taken are presented in Figure 3(k). Under lower magnification (Figure 3(k(i-iii)), the silver nanocomposite structures appear round, with a range of lattice spacings corresponding to (004) plane Ag (2.5 Å, JCPDS PDF#:41-1402) and (200) plane Ag_2O (2.6 Å, JCPDS PDF#:41-1104). The SAED pattern obtained from the lasered sample is presented in Figure 3(k(vi)). The bright spots arranged in a ring pattern indicate a polycrystalline structure with differing crystal orientations.

The XPS spectra of the lasered sample are presented in Figure 3(l-n). Peaks attributed to 3d3 and 3d5 electrons in elemental silver were obtained. Remarkably, there were no peaks attributed to Ag-O bonding electrons obtained. After laser patterning, there was a decrease in the percentage of O 1s electrons involved in O-Fe bonding from 38.2 to 16.4, as well as a decrease in the percentage of Fe 2p electrons in Fe_2O from 16.0 to 13.2, indicating that bonds were broken within the Fe_2O_3 substrate.

3.4 Proposed Mechanism

Based on the characterisation conducted, the following mechanism for the formation and fluorescence phenomenon of the $Ag-Fe_2O_3$ nanocomposite structure is proposed:

The Fe_2O_3 nanoflakes absorb energy from the 532 nm laser beam, which falls within their absorption spectrum[21], and convert it to heat. This photothermal process, as described in equation (1), results in the partial melting of the tips of the nanoflakes, forming O^{2-} and Fe^{3+} ions in solution:

$$Fe_2O_3(s) \longrightarrow 2Fe^{3+}(aq) + 3O^{2-}(aq) \quad (1)$$

Within the immediate surrounding of the nanoflakes, there is a high concentration of O^{2-} ions, which causes silver oxides to precipitate from the solution and form nanoparticles that are anchored onto the Fe_2O_3 nanoflakes:

$$2Ag^{+}(aq) + O^{2-}(aq) \longrightarrow 2AgO(s) \quad (2)$$

$$4Ag^{+}(aq) + O^{2-}(aq) \longrightarrow 2Ag_2O(s) \quad (3)$$

The silver oxides are sensitive to light, and the surface layer will readily decompose into Ag:

$$2AgO(s) \longrightarrow 2Ag(s) + O_2(g) \quad (4)$$

$$2Ag_2O(s) \longrightarrow 4Ag(s) + O_2(g) \quad (5)$$

This process is summarised in Figure 4(a). A further observation that supports the proposed mechanism is the consistent formation of air bubbles, such as in Figure 4(b), after a prolonged period of lasering. The diffused (unfocused) laser spot seen in time t = 2 s - 10 s is due to the refraction of the laser beam as it passes through an air bubble, and was observed after 150 s of laser patterning. A video of the bubble formation process can be found in the supplementary information V1. The possibility that the air bubbles are merely due to the solution boiling is ruled out by repeating the laser patterning process under de-ionised water, which did not produce such air bubbles even after protracted periods of laser treatment. A video of this can be found in supplementary information V2. This formation mechanism also explains the presence of silver oxides detected in the Raman spectroscopy but not in the XPS, as the Raman excitation has a deeper probe depth (100 μm) than the XPS (< 100 Å), and the photodecomposition in equations (4) and (5) will only affect the surface layer of silver oxides.

The fluorescence mechanism of the nanocomposite can be explained *via* the Fe_2O_3 nanoflakes' inherent fluorescence and the nano silver deposition's enhancement effect.

Figure 4(c) shows the PL spectrum of the lasered and pristine sample, under 532 nm excitation. The samples exhibited the strongest emission peak centred at 691 nm. However, the intensity is greatly strengthened in the lasered sample, which supports the suggestion that incorporating Ag mainly enhances the fluorescence already associated with the Fe_2O_3 nanoflakes. According to Shi *et al* (2015)[22] and Sadat *et al* (2014)[23], an emission of around 690 nm is associated with the recombination of trapped electrons from the octahedral site to O(2p) in crystalline Fe_2O_3 (Figure 4(d)).

The validity of the proposed mechanism is justified by repeating similar laser treatment of the Fe_2O_3 nanoflakes in de-ionised water. The results are reported in Figure 4(e-h). As shown in Figure 4(e-f), without Ag present, there is no enhancement of the underlying red fluorescence. In fact, notably, the lasered sample region appears noticeably dimmer than the surrounding regions. Observing the same lasered square under the SEM (Figure 4(g) and (h), it can be seen that lasering under de-ionised water had caused the Fe_2O_3 substrate's flake-like surface to melt and flatten into a smoothened one. This would have increased the characteristic length of the nanoflakes greatly and may have caused its innate fluorescence, which have been reported to be size-dependent[24], to decrease or disappear.

4 Applications

During characterisation, it was discovered that after conducting EDX analysis on a laser-patterned square, the area treated with electrons shows an increased in fluorescence intensity while the neighbouring regions did not.

To prove that this effect is in fact due to the electron irradiation, a large lasered sample was prepared, and a copper (Cu) TEM grid was placed over the lasered region (Figure 5(a)). The grid serves as a mask that blocks electrons from interacting with the regions of the lasered sample below the grid lines, leaving only regions in the grid gaps exposed to electron irradiation. EDX elemental map shows that the grid is mapped to the element Cu, while the exposed region only indicates the presence of Ag and Fe (Figure 5(b-c)). After this preparation, the sample is placed under the SEM's high-energy electron beam (Figure 5(d)). In doing so, one would expect the electron-bombarded $Ag-Fe_2O_3$ nanocomposite located in the grid gaps to emit stronger fluorescence under yellow excitation. In other words, removing the TEM mask will allow an "invisible" mask to be observable based on the fluorescence contrast.

Indeed, before the electron treatment, the laser-patterned region exhibits a uniform distribution of bright blue specks under bright field and uniform red fluorescence under yellow wavelength excitation (Figure 5(e)). After electron treatment, no grid pattern is observed under BF imaging. However, the intensity of the red fluorescence under yellow excitation was found to increase only in the exposed areas of the sample. As a result, an invisible mask highlighting a "crosshatch" pattern comprising regions with various intensities of red fluorescence is formed (Figure 5(f)).

This effect was quantitatively understood by repeating the electron bombardment process with different electron dosages and observing the fluorescence changes. Electron dosage is defined as:

$$\text{Dose} = \frac{It}{A} \quad (6)$$

Where I is the current, t is the duration of the irradiation, and A is the dosed area.

1 dose is defined as 2.55×10^6 Cm^2, and was achieved through directing a high-energy beam of 15 keV and current 15 μA on a

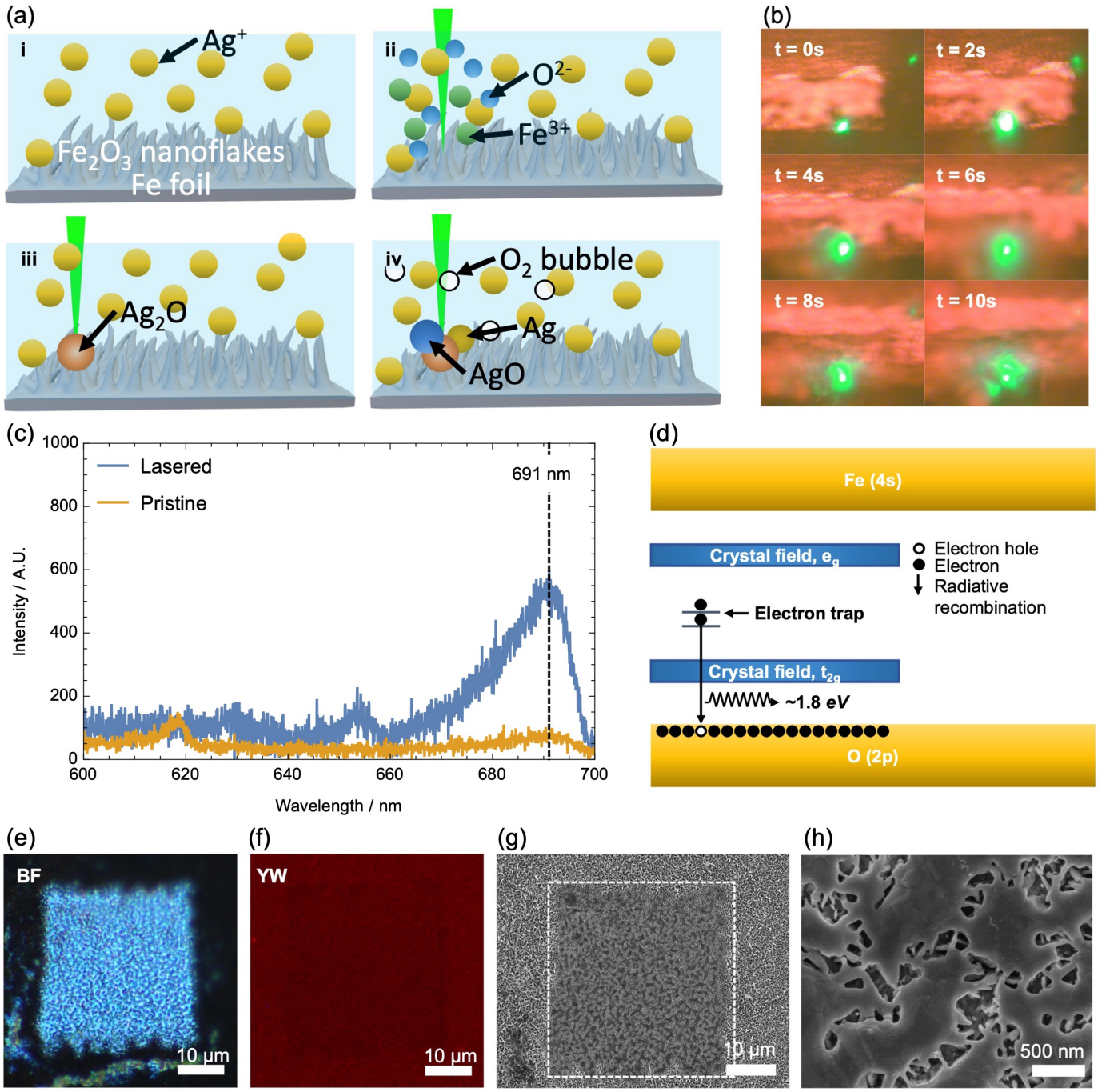

Fig. 4 (a) Labelled 3D schematic of proposed mechanism for the formation of the Ag–Fe_2O_3 composite. (b) Screengrabs (within 10 seconds) of laser patterning of Fe_2O_3 nanoflakes under $AgNO_3$ (aq) where the formation of an air bubble is observed. (c) PL spectra of the lasered and pristine squares. (d) Energy level diagram showing the proposed electronic transition responsible for fluorescence emission. (e) FM images of a micro-square lasered under de-ionised water observed under bright field and (f) yellow excitation. (g-h) SEM images of micro-square lasered under de-ionised water taken at lower and higher magnifications. Dotted square in (g) highlights the location of the laser-patterned region. (h) Higher magnification SEM image taken within the laser patterned region.

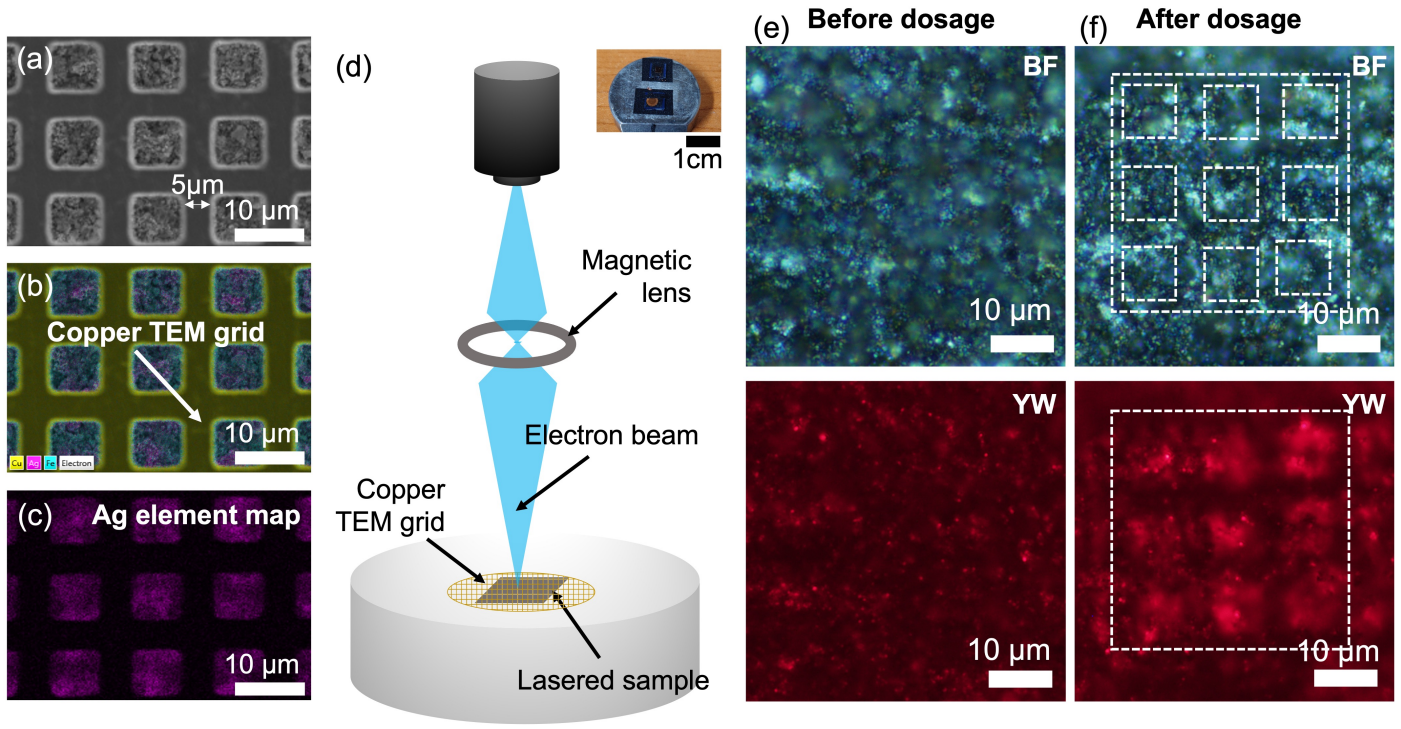

Fig. 5 (a) SEM image of the copper TEM grid mask being placed over a large area of Ag−Fe_2O_3 nanocomposite. (b) EDX element map of Ag, Cu and Fe overlaid on SEM image of the copper TEM grid placed over sample. (c) Ag element map highlighting the Ag element's presence only within the grid's exposed region. (d) A 3D schematic of electron dosage set-up. (e-f) Ag−Fe_2O_3 composite (e) before and (f) after electron dosage under BF (above) and yellow (below) excitation. Dotted lines inset on (f) serve a a visual guide to highlight the original masked region.

30.0 μm x 53.3 μm area for 6.36 mins. The fluorescence intensity is quantified by integrating the area under the fluorescence spectrum graph. FM images of a set of squares before and after varying dosages of electrons are shown in Figure 6(a), while the percentage change in the fluorescence intensity against electron dosage is plotted in Figure 6(b). The percentage increase in fluorescence brightness shows an increasing trend with electron dosage. The experiment is repeated twice to ensure repeatability, with the results showing a similar increasing trend. These results are presented in the supplementary information, Figure S2.

To achieve a fundamental understanding of the aforementioned phenomenon, XPS analyses are conducted on the electron-treated sample (Figure 6(c-e)). The spectra for the lasered but not electron-treated sample are also plotted on the same axes in dashed lines to aid in comparison. It is determined that after electron bombardment, the Ag 3ds and 5ds peaks shifted to a higher binding energy. Since Ag in metallic form is known to exhibit a higher binding energy relative to silver oxide[25], such a shift could indicate the reduction of silver oxides into metallic silver taking place when the sample is treated with high-energy electrons.

The process of electron-initiated transformation of silver oxide to silver is observed under TEM imaging. By capturing a series of TEM images of the same region over a period of time, in-situ transformation of Ag_2O to Ag in the presence of electron bombardment is arrested by capturing how the crystallinity of Ag_2O changes. The laser-patterned sample is transferred onto a TEM grid, and multiple consecutive images are captured. The series of images taken is presented in Figure 6(f) where white/red dotted boxes are included as a visual guide to highlight the transformation of amorphous AgO (white dotted boxes) to crystalline Ag (red dotted boxes).

At 0 min (Figure 6(f(i))), regions within the four white dotted boxes begin in an amorphous state. After 1 min (Figure 6(f(ii))) and 2 mins (Figure 6(f(iii))) of electron bombardment, lattice structures with spacings corresponding to 2.5 Å are visible in the two outermost regions (highlighted by the red boxes). The spacing corresponds to the (004) plane of Ag (JCPDS PDF #: 41-1402). With 7 mins of electron interactions (Figure 6(f(iv))), the crystalline region extended from the inner region towards the outer region. The newly transformed region also has a lattice spacing of 2.5 Å. At 9 mins (Figure 6(f(v))), the region of interest has fully converted from an amorphous state to a crystalline state, with the entire region composed of an orderly lattice of crystalline Ag with a lattice spacing of 2.5 Å. The crystallinity remains stable even after an addition 2 mins (Figure 6(f(vi))) of electron bombardment. This suggests that the electron dose has led to the formation of Ag from the amorphous material, which is likely to be a mixture of Ag_nO compounds formed during laser patterning. As silver metal but not oxides of silver can enhance fluorescence *via* surface plasmon resonance, the conversion of the surface silver oxide nanostructures into silver readily explains the observed enhancement of the red fluorescence.

5 Conclusions

In summary, this work presents an alternative way to synthesise Ag−Fe_2O_3 composite nanostructures using a focused laser

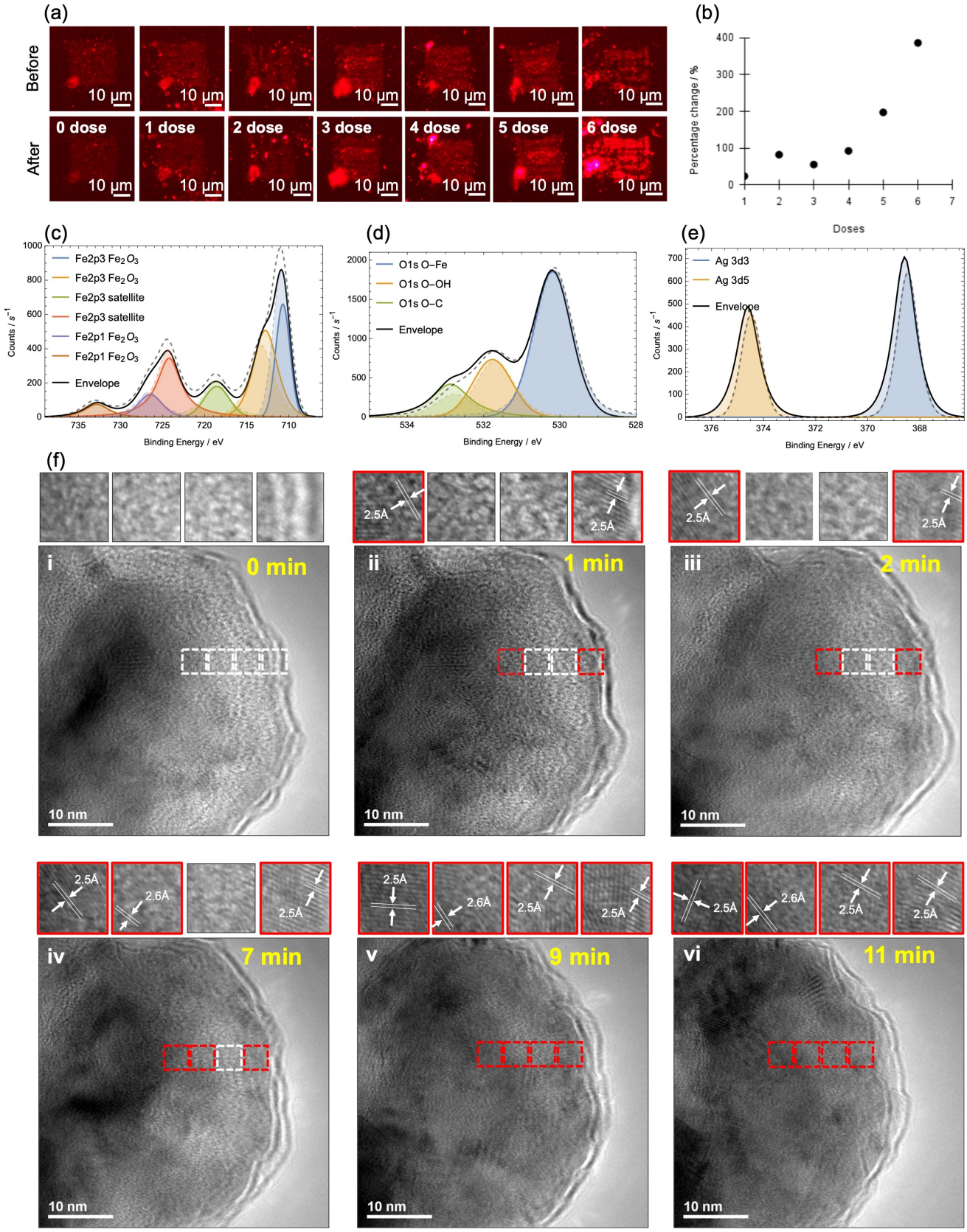

Fig. 6 (a) Lasered sample before (above) and after (below) electron bombardment. (b) Plot of percentage change of fluorescence intensity against electron dosage. (c-e) XPS spectrum of Fe2p, (d) O1s, and (e) Ag3ds scans of the electron-treated sample. The spectrum for the laser-treated but not electron-treated sample is also plotted on the same axes in dashed lines to aid in comparison. (f) HRTEM images of the same region of a lasered sample after (i) 0 min, (ii) 1 min, (iii) 2 mins, (iv) 7 mins, (v) 9 mins, and (vi) 11 mins of electron bombardment.

beam. Submerging the Fe_2O_3 nanoflake substrate in a solution full of silver ions, while introducing a focused laser beam onto the sample, causes the Fe_2O_3 nanoflakes to generate localised heat, which facilitates photothermal reduction of Ag ions at the specific site. This leads to the uniform and site-selective formation of the $Ag-Fe_2O_3$ nanocomposite in the lasered region. Uniquely, bright red fluorescence from the composite is observed and attributed to the Ag nanostructure's enhancement of the Fe_2O_3's intrinsic fluorescence through surface plasmon resonance effects. Such an optical phenomenon not only allows facile, direct visual determination of the formation and change in oxidation state of the Ag nanostructure, but it also enables the $Ag-Fe_2O_3$ nanocomposite to function as an effective micro-beta particle detector with real-time optical feedback. Looking forward, the development of alternative synthesis processes is a viable path towards unravelling non-traditional applications of nanocomposites.

Author contributions

Yue Yin: Writing - review and editing, Writing - original draft, Methodology, Investigation, Formal analysis, Data curation. **Aseera Jannath:** Writing - original draft, Methodology, Investigation, Data curation. **Zheng Zhang**: Methodology, Investigation. **Sharon Xiaodai Lim:** Writing - review and editing, Writing - original draft, Supervision, Project administration, Conceptualisation. **Chorng Haur Sow**: Writing - review and editing, Writing - original draft, Supervision, Resources, Project administration, Conceptualisation

Conflicts of interest

There are no conflicts to declare.

Data availability

The data supporting this article have been included in the Supplementary Information.

Acknowledgements

The authors acknowledge the generous support from the Singapore MOE-ARC grant (A-8001494-00-00).

Notes and references

1 M. K. Hossain, A. Mishra, A. Tiwari, B. Pant, S. C. Dey, A. Tiwari, O. Saha, M. M. Rahaman, Y. R. Shukla, A. Tiwari and M. Ashaduzzaman, *SN Appl. Sci.*, **5**, 339.

2 M. A. Rabbi, M. B. Akter, B. M. Chaki, M. A. Latif, M. Al-Amin, M. Z. U. Rasel, S. Sharmin, M. Abdurrahim, M. H. K. Rubel and M. R. Habib, *New J. Chem.*, **48**, 5278–5288.

3 S. A, A. Thamer, R. K, P. A, R. V, M. K, A. Murad and M. P, *Journal of Photochemistry and Photobiology B: Biology*, **207**, 111885.

4 A. Mirzaei, K. Janghorban, B. Hashemi, A. Bonavita, M. Bonyani, S. G. Leonardi and G. Neri, *Nanomaterials (Basel)*, **5**, 737–749.

5 S. Liu, Y. Chen and L. Dong, *Mater. Res. Express*, **3**, 075024.

6 V. T. Trang, L. T. Tam, V. N. Phan, N. Van Quy, T. Q. Huy and A.-T. Le, *Journal of Electronic Materials*, **46**, 3323–3332.

7 K. Nasiri, **8**, 283–289.

8 F. A. M. Al-Zahrani, S. S. Salem, H. A. Al-Ghamdi, L. M. Nhari, L. Lin and R. M. El-Shishtawy, *Bioengineering (Basel)*, **9**, 452.

9 F. A. M. Al-Zahrani and R. M. El-Shishtawy, **13**, year.

10 N. S. Mohan, R. Gokulkumar, J. Shankar, R. Sridharan, B. Logesh, R. Sasikumar, K. Vallarasu and V. Vijayalakshmi, *Results in Chemistry*, **4**, 100626.

11 Z. Chai, A. Childress and A. A. Busnaina, *ACS Nano*, **16**, 17641–17686.

12 T. Yu, Y. Zhu, X. Xu, K.-S. Yeong, Z. Shen, P. Chen, C.-T. Lim, J. T.-L. Thong and C.-H. Sow, *Small*, **2**, 80–84.

13 H. Mansour, H. Letifi, R. Bargougui, S. De Almeida-Didry, B. Negulescu, C. Autret-Lambert, A. Gadri and S. Ammar, *Applied Physics A*, **123**, 787.

14 P. Kumar, H. No-Lee and R. Kumar, *J Mater Sci: Mater Electron*, **25**, 4553–4561.

15 M. Lübbe, A. M. Gigler, R. W. Stark and W. Moritz, *Surface Science*, **604**, 679–685.

16 D. Bersani, P. P. Lottici and A. Montenero, *Journal of Raman Spectroscopy*, **30**, 355–360.

17 A. M. Jubb and H. C. Allen, *ACS Appl. Mater. Interfaces*, **2**, 2804–2812.

18 C. A. Schneider, W. S. Rasband and K. W. Eliceiri, *Nature Methods*, **9**, 671–675.

19 U. Agarwal, R. Reiner and J. Beecher, 15th International Symposium on Wood, Fiber, and Pulping Chemistry, 2009.

20 R. Nagiri, *PhD thesis*, IIT Madras, 2011.

21 J. Cai, S. Li, H. Pan, Y. Liu and G. Qin, *J Mater Sci*, **51**, 8148–8155.

22 D. Shi, M. E. Sadat, A. W. Dunn and D. B. Mast, *Nanoscale*, **7**, 8209–8232.

23 M. Sadat, M. Kaveh, A. Dunn, H. Wagner, R. Ewing, J. Zhang, H. Xu, G. Pauletti, D. Mast and D. Shi, *Applied Physics Letters*, 2014, **105**, 091903.

24 Y. Zhang, W. Liu, C. Wu, T. Gong, J. Wei, M. Ma, K. Wang, M. Zhong and D. Wu, *Materials Research Bulletin*, **43**, 3490–3494.

25 A. M. Ferraria, A. P. Carapeto and A. M. Botelho do Rego, *Vacuum*, **86**, 1988–1991.

Supplementary Information

Laser Initiated Site-selective Formation of Fluorescing Ag-Fe_2O_3 Nanocomposites for Electron Detection

Yue Yin[a], Aseera Jannath[a], Zheng Zhang[b], Chorng Haur Sow*[c], Sharon Xiaodai Lim*[c]

[a] Raffles Institution, 1 Raffles Institution Lane, Singapore 575954.

[b] Institute of Materials Research and Engineering (IMRE), Agency for Science, Technology and Research (A*STAR), 2 Fusionopolis Way, Innovis #08-03, Singapore 138634, Singapore

[c] Department of Physics, National University of Singapore, 2 Science Drive 3, Singapore 117542

*Address correspondence to Dr. Sharon Xiaodai Lim. E-mail: phylimx@nus.edu.sg and Prof. Chorng Haur Sow. E-mail: physowch@nus.edu.sg.

Content

Image processing pipeline for analysing the size of the silver-containing deposits

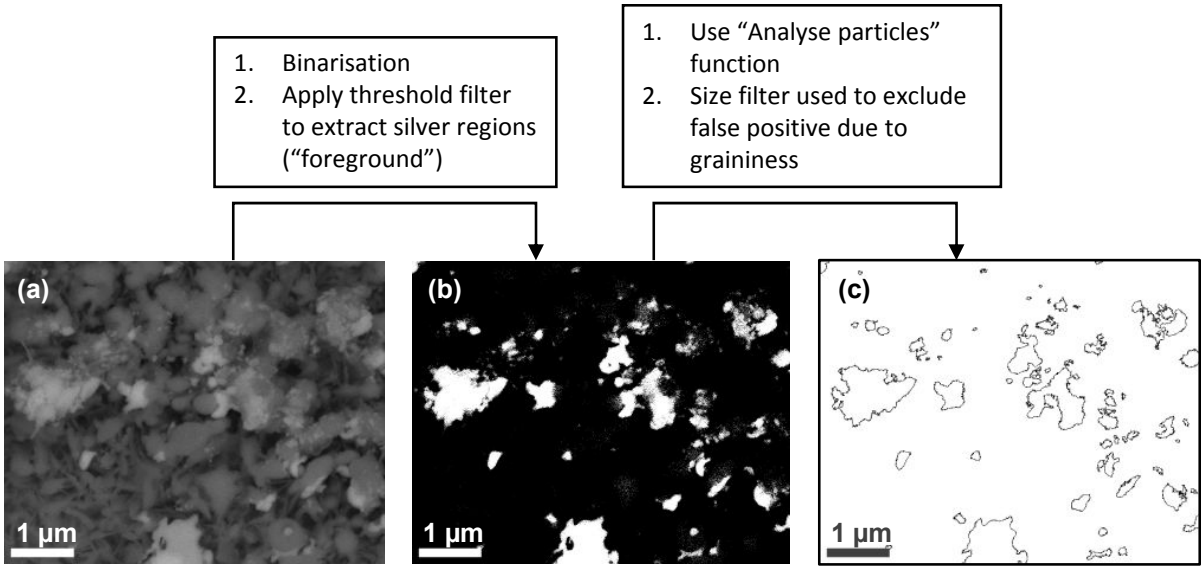

Supplementary Fig. 1. (a) Backscattered electron image of lasered region, (b) Image with threshold filter applied, (c) Mask of particles identified.

Graphs of change in fluorescence intensity against electron treatment dosage

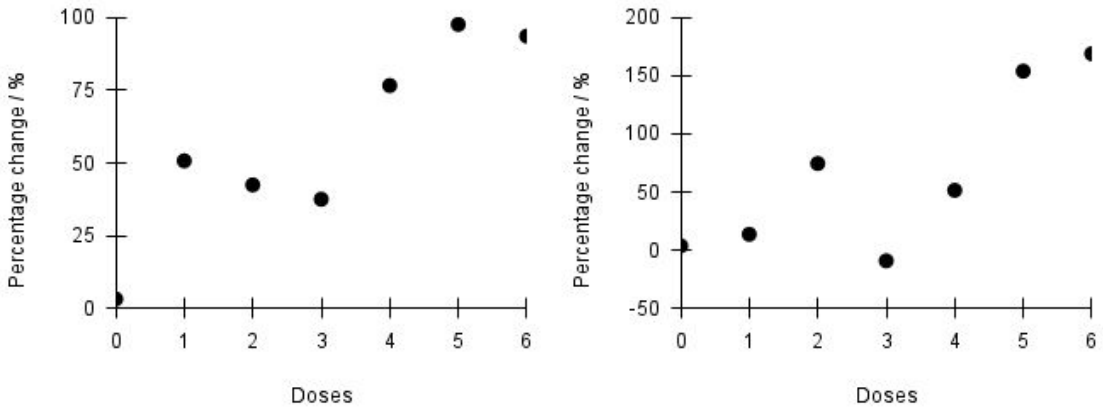

Supplementary Fig. 2. Plot of percentage change in fluorescence intensity against electron dosage, showing increasing trend.

Supplementary Vid. 1. An 11 second screen capture video of the bubble formation process when lasering under $AgNO_3$ solution. Initially the laser is in focus and a small green laser spot can be seen. At t = 2 seconds, bubbles begin to form. Visually, the formation of the bubbles can be identified as it causes the laser spot to become bigger and more diffuse.

Supplementary Vid. 2. A 89 second screen capture video of lasering under deionised (DI) water. No bubbles are formed despite the long period of lasering.

Table of Content

Laser Initiated Site-selective Formation of Fluorescing Ag-Fe_2O_3 Nanocomposites for Electron Detection

Yue Yin, Aseera Jannath, Zheng Zhang, Chorng Haur Sow, Sharon Xiaodai Lim**

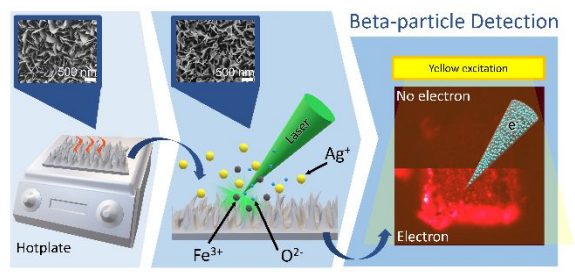

Laser-initiated Ag-Fe_2O_3 emits unique red fluorescence whose intensity enhances 10x upon electron interaction, enabling rapid optical response to electron detection.